Symposium on Thermoacoustics in Combustion: Industry meets Academia (SoTiC 2023)
Sept. 11 - Sept. 14, 2023
Zürich, Switzerland

Shape Sensitivities for Thermoacoustic Stability of Annular Combustors

Ekrem Ekici[1] and Matthew P. Juniper[1]

Abstract

Modern gas turbine combustors are susceptible to oscillations caused by the interaction between sound waves and the flame. If the acoustic pressure is sufficiently in phase with the heat release rate, the oscillations can grow significantly, which may cause extra heat transfer, excessive noise, or even failure of the engine. We use the thermoacoustic Helmholtz equation to model this instability problem as an eigenvalue problem. The eigenfrequency and the growth rate of the system are obtained using a finite element based Helmholtz solver by defining the geometry and system parameters as well as by imposing the acoustic boundary conditions and fluctuating body forces. After calculating the eigenvalue and eigenvector of the problem, we use adjoint methods to calculate the sensitivity of the eigenvalue to changes in the shapes of the surfaces of the combustor geometry. We demonstrate the application of this procedure to an example annular combustor with dilution holes for two different eigenmodes. The computed shape sensitivity fields can guide design changes that will improve the stability of the combustor.

Keywords

Thermoacoustic instability, adjoint methods, Helmholtz solver, shape optimization

Introduction

Thermoacoustic instability is a major problem that threatens the sustainable operability of gas turbine engines. Growing acoustic oscillations in the combustor chamber can lead to detrimental vibrations that increase the fatigue of engine components. These oscillations are extremely sensitive to minor changes in some system parameters, such as operating point, fuel composition and system geometry (1). Therefore, relatively cheap and accurate tools are desirable to examine the influences of the design parameters.

To determine the sensitivity to the system parameters, adjoint methods can be used (2). With adjoint methods, the behaviour of the eigenvalue with respect to the system parameters can be calculated cheaply. In addition to the operating parameters, geometrical parameters of the combustor can be considered. The motivation is that small modifications to the geometry could lead to passive control of the system (3). A low-order network model is used in (4) to stabilize the unstable modes of a longitudinal combustor by changing its shape, informed by adjoint methods. However, low-order thermoacoustic network models are limited to relatively simple combustor geometries. For this reason, Helmholtz solvers are better suited to evaluate more complex geometries with the cost of increased computational effort. In Helmholtz solvers, the mean flow is assumed to be zero, and the fluctuating heat release rate is modelled as a distributed acoustic source.

In this study, we calculate the sensitivity of the thermoacoustic eigenmodes to changes in an annular combustor geometry using an adjoint Helmholtz solver. We use the finite element method to handle the complex geometry and we model the damping caused by the dilution holes as a fluctuating body force within the holes. The derivation of this model is presented in detail. The choked boundary conditions are implemented and incorporated into the Helmholtz solver to account for additional damping on choked boundaries. The nonlinear eigenvalue problem is solved using fixed point iteration. The direct and adjoint eigenfunctions of eigenmodes are used to calculate the shape derivatives of the combustor boundaries (5).

Methodology

Thermoacoustic Helmholtz equation

The derivation of the direct and adjoint thermoacoustic Helmholtz equations follows the methodology in (5). The direct Helmholtz equation and momentum equation are

$$\nabla \cdot \left(c^2 \nabla \hat{p}_1\right) + \omega^2 \hat{p}_1 = +i\omega(\gamma - 1)\hat{q}_1 + c^2 \nabla \cdot \hat{f}_1 + c^2 i\omega \hat{m}_1, \tag{1a}$$

$$-i\rho_0 \omega \hat{\mathbf{u}}_1 + \nabla \hat{p}_1 = \hat{f}_1, \tag{1b}$$

where c is the spatially-varying speed of sound, $\hat{p}_1$ is the acoustic pressure, $\hat{\mathbf{u}}_\mathbf{1}$ is the acoustic velocity, ω is the complex valued angular frequency, γ is the heat capacity ratio, $\hat{q}_1$ is any fluctuating heat release rate, $\hat{f}_1$ is any fluctuating body force, $\hat{m}_1$ is any fluctuating mass injection and p_0 is the mean pressure. Eq. (1) can be written as $\mathcal{L}(\omega)\hat{p} = 0$, where $\mathcal{L}$ is a differential operator that is linear in $\hat{p}_1$ but potentially nonlinear in ω. The local $n - \tau$

[1]Cambridge University Engineering Department, Cambridge, CB2 1PZ, UK

Corresponding author:
Matthew Juniper, Department of Engineering, University of Cambridge, Cambridge CB2 1PZ, UK.
Email: mpj1001@cam.ac.uk

formulation is used to model the heat release rate caused by the unsteady flame response:

$$\frac{q_1(\mathbf{x},t)}{q_{tot}} = \frac{nh(\mathbf{x})\int_\Omega w(\mathbf{x})\mathbf{u}_1\left(\mathbf{x},t-\tau(\mathbf{x})\right)\cdot\mathbf{n}_r d\mathbf{x}}{u_b} \tag{2}$$

where q_{tot} is the mean heat release rate, n is the interaction index, u_b is the mean velocity, τ is the time delay and $\mathbf{n}_r$ is the unit normal vector in the reference direction. $h(\mathbf{x})$ and $w(\mathbf{x})$ are the heat release rate distribution and measurement function fields, which are modified Gaussian functions integrating to 1 over the domain.

With the definition $\langle\hat{p}_1^\dagger|\mathcal{L}\hat{p}_1\rangle = 0$, the adjoint Helmholtz equation and momentum equations are (5)

$$\nabla\cdot\left(c^2\nabla\hat{p}_1^\dagger\right) + \omega^{*2}\hat{p}_1^\dagger = -i\omega^*(\gamma-1)\hat{q}_1(\omega^*) - c^2\nabla\cdot\hat{f}_1 - i\omega^*\gamma p_0\hat{m}_1, \tag{3a}$$

$$-i\rho_0\omega^*\hat{\mathbf{u}}_1 + \nabla\hat{p}_1^\dagger = \hat{f}_1. \tag{3b}$$

where $\hat{p_1}^\dagger$ is the adjoint eigenfunction and w^* is the complex conjugate of the angular eigenfrequency.

Boundary conditions

Three types of acoustic boundary conditions are used; Dirichlet, Neumann and Robin conditions. For annular combustors, most of the walls are Neumann ($\nabla\hat{p}\cdot\mathbf{n}=0$) boundaries or choked boundary conditions. The reflection coefficient of the inlet choked boundary condition is

$$R_i = \frac{1-\gamma_i M_i/(1+(\gamma_i-1)M_i^2)}{1+\gamma_i M_i/(1+(\gamma_i-1)M_i^2)}, \tag{4}$$

where γ_i is the heat capacity ratio on the inlet choked boundary and M_i is the Mach number near the downstream of the inlet choked boundary. Similarly, we write the choked outlet condition as

$$R_o = \frac{1-(\gamma_o-1)M_o/2}{1+(\gamma_o-1)M_o/2}, \tag{5}$$

where γ_o is the heat capacity ratio on the outlet choked boundary and M_o is the Mach number near the upstream of the outlet choked boundary. These reflection coefficients can be imposed on Robin boundaries through the specific impedance, $Z=(1+R)/(1-R)$:

$$\nabla\hat{p}_1\cdot\mathbf{n} - \frac{iw}{cZ}\hat{p}_1 = 0 \tag{6}$$

for the direct solution and

$$\nabla\hat{p}_1^\dagger\cdot\mathbf{n} - \frac{iw^*}{cZ}\hat{p}_1^\dagger = 0 \tag{7}$$

for the adjoint solution.

Damping model for dilution holes

Acoustic dissipation due to flow separation occurs through the dilution holes connecting the cooling duct and combustion chamber in the annular combustors. The Helmholtz solver cannot model flow separation so its influence is modelled physically and included as a body force.

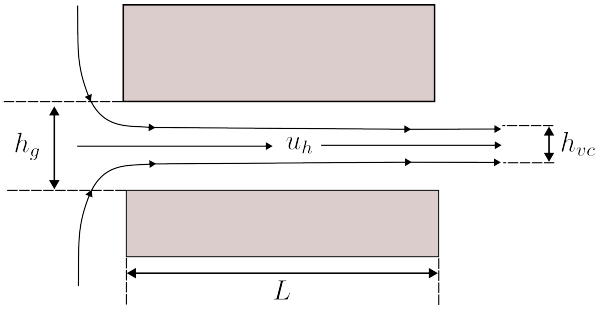

Figure 1. Schematical representation of the modified Cummings model

The modified Cummings model in (6) is used (Fig. 1).

$$L\frac{d\mathbf{u_1}}{dt} + \frac{\mathbf{u_1}u_h}{\sigma^2} = \frac{p_I}{\rho_0} \tag{8}$$

Eq. (8) represents the aeroacoustic model in which L is the length of the dilution hole, u_h is the mean velocity in the hole, $\sigma = h_{vc}/h_g$ is the contraction ratio, p_I is the pressure difference across the hole and ρ_0 is the mean density. The fluctuating body force f_1 has units of force per unit volume (Nm^{-3}). We write

$$f_1 = \frac{(p_I)S_n}{S_n L} = \frac{p_I}{L} = \rho_0\frac{\partial\mathbf{u}_1}{\partial t} + \frac{\rho_0 u_h\mathbf{u}_1}{\sigma^2 L}, \tag{9}$$

where S_n is the cross-sectional area of the dilution hole. Eq. (9) in the frequency domain is:

$$\hat{f}_1 = -i\omega\rho_0\hat{\mathbf{u}}_1 + \frac{\rho_0 u_h\hat{\mathbf{u}}_1}{\sigma^2 L}. \tag{10}$$

If we take the divergence of Eq. (10), we obtain

$$\nabla\cdot\hat{f}_1 = -i\omega\rho_0\nabla\cdot\hat{\mathbf{u}}_1 + \frac{\rho_0 u_h\nabla\cdot\hat{\mathbf{u}}_1}{\sigma^2 L}. \tag{11}$$

In Eq. (11), the divergence of the acoustic velocity inside the hole can be found by taking the divergence of (1b);

$$-i\rho_0\omega\nabla\cdot\hat{\mathbf{u}}_1 + \nabla^2\hat{p}_1 = \nabla\cdot\hat{f}_1. \tag{12}$$

To obtain $\nabla\cdot\hat{\mathbf{u}}_1$, we substitute Eq. (11) into (12);

$$\nabla\cdot\hat{\mathbf{u}}_1 = \frac{\sigma^2 L}{\rho_0 u_h}\nabla^2\hat{p}_1, \tag{13}$$

and we substitute Eq. (13) into Eq. (11) to obtain the divergence of the body force in terms of the acoustic pressure;

$$\nabla\cdot\hat{f}_1 = -i\omega\frac{\sigma^2 L}{u_h}\nabla^2\hat{p}_1 + \nabla^2\hat{p}_1. \tag{14}$$

This is substituted into Eq. (1) such that the effect of flow separation is modelled as a body force within the hole.

Finite element discretization

Within the finite element framework, we integrate the terms in (3a) over the domain and multiply by a test function v to

obtain

$$\int_\Omega \nabla\cdot\left(c^2\nabla\hat{p}_1\right)\cdot v\,\mathbf{dx}+\int_\Omega \omega^2\hat{p}_1\cdot v\,\mathbf{dx}= -\int_\Omega i\omega(\gamma-1)\hat{q}_1\cdot v\,\mathbf{dx} -\int_{\Omega_h} c^2(-i\omega\frac{\sigma^2 L}{u_h}\nabla^2\hat{p}_1+\nabla^2\hat{p}_1)\cdot v\mathbf{dx}_h. \quad (15)$$

Note that the final term in Eq. (3a) is only integrated over the domain in which the fluctuating body force f acts. The subscript $_h$ denotes hole. We use trial functions ϕ_i such that $\hat{p}_1=\sum_i \phi_i\cdot p_{1,i}$. Integrating the terms in Eq. (15) by parts gives

$$\sum_i\Big(-\int_\Omega c^2\nabla\phi\cdot\nabla v\,\mathbf{dx}+\int_{\partial\Omega} c^2\nabla\phi\cdot\mathbf{n}\,v\,dS +\int_\Omega \omega^2\phi\cdot v\,\mathbf{dx}\Big)p_{1,i}=\sum_i\Big(-\int_\Omega i\omega(\gamma-1)\hat{q}_1\cdot v\,\mathbf{dx} -\int_{\Omega_h} c^2 i\omega\frac{\sigma^2 L}{u_h}\nabla\phi\cdot\nabla v\,\mathbf{dx}_h +\int_{\partial\Omega_h} c^2 i\omega\frac{\sigma^2 L}{u_h}\nabla\phi\cdot\mathbf{n}\cdot v\,\mathbf{dS}_h +\int_{\Omega_h} c^2\nabla\phi\cdot\nabla v\,\mathbf{dx}_h-\int_{\Omega_h}\nabla\phi\cdot\mathbf{n}\cdot v\,dS_h\Big)p_{1,i}, \quad (16)$$

where $\mathbf{n}$ is the normal vector of the relevant boundary. We can transform the second integral in Eq. (16) into the Robin integral using Eq. (1b). The matrix form of Eq. (16) is

$$\left[\mathbf{A}+\omega\mathbf{B}+\omega^2\mathbf{C}\right]\mathbf{p}=\mathbf{D}(\omega)\mathbf{p} \quad (17)$$

where

$$\mathbf{A}=-\int_\Omega c^2\nabla\phi\cdot\nabla v\,\mathbf{dx}-\int_{\Omega_h} c^2\nabla\phi\cdot\nabla v\,\mathbf{dx}_h, \quad (18a)$$

$$\mathbf{B}=\int_{\partial\Omega}\frac{ic}{Z}\phi\cdot v\,dS+\int_{\Omega_h} c^2\frac{\sigma^2 iL}{u_h}\nabla\phi\cdot\nabla v\,\mathbf{dx}_h -\int_{\partial\Omega_h}\frac{ic\sigma^2 L}{u_h Z}\phi\cdot v\,\mathbf{dS}_h, \quad (18b)$$

$$\mathbf{C}=\int_\Omega \phi\cdot v\,\mathbf{dx}, \quad (18c)$$

$$\mathbf{D}=\int_\Omega(\gamma-1)\eta\,\phi\,h\,e^{i\omega\tau}\mathbf{dx}\otimes\int_\Omega\frac{w}{\rho_0}\nabla v\cdot\mathbf{n}_r\mathbf{dx} \quad (18d)$$

and $\mathbf{p}$ is the direct eigenvector. In Eq. (18d), $\eta=nq_{tot}/u_b$ and the operator $\otimes$ performs the outer product between the left integral and the right integral. To derive the adjoint in matrix form, we take the conjugate transpose of Eq. (18) and calculate the right eigenvector to give the adjoint eigenvector.

Shape Derivatives

The shape sensitivities for the thermoacoustic Helmholtz equation are derived in (5). The most general expression for the shape derivative is that of the Robin boundary;

$$\omega'=\int_\Gamma C\Bigg(-\hat{p}^{\dagger^*}\Big(\kappa c^2\frac{\partial c}{\partial n}\Big)\frac{\partial\hat{p}}{\partial n}+\nabla\cdot\Big(\hat{p}^{\dagger^*}c^2\nabla\hat{p}\Big) -2\frac{\partial\hat{p}^{\dagger^*}}{\partial n}c^2\frac{\partial\hat{p}}{\partial n}\Bigg)dS \quad (19)$$

where $C=1/A_b$ is used to displace the relevant boundaries with the surface area A_b in the normal direction. When applying Neumann boundaries, we impose $\partial\hat{p}_1/\partial n=0$ and $\partial\hat{p}_1^\dagger/\partial n=0$.

As we compute the gradient information in the direction of the outward normal vector of the pertinent boundary, the significance of the complex component of the shape gradient becomes pivotal. In cases where the computed mode is unstable and the complex part of the shape derivative on the boundary bears a negative sign, translating the boundary in the direction of the outward normal vector becomes necessary to stabilize the system. Conversely, when dealing with a stable calculated mode and a positive complex component of the shape gradient along the boundary, moving the boundary along the outward normal vector's direction is required for further stabilization.

Helmholtz solver

The three dimensional computational grid with 250,000 cells is generated by Gmsh (7) using Delaunay triangulation. The finite element model is built with the open-source platform DOLFINx (8) using P2 continuous Galerkin elements. The weak forms in Eq. (18) are defined using the UFL package (9). All the matrices in Eq. (18) are assembled within the subroutines of DOLFINx apart from the active flame matrix. This matrix is implemented using the PETSc package (10) explicitly. The PEP solver in the SLEPc package (11) is used to determine the nonlinear quadratic eigenvalue problem (Eq. (17)). The shift-and-invert spectral transformation is exploited to enhance the convergence of the eigenvalue to the initial guess. Fixed point iteration with relaxation is implemented in order to converge to the eigenvalue (12). The solver parallelizes with the OpenMPI library (13).

Results

Annular combustor geometry

The three dimensional view of the example annular combustor geometry is shown in Fig. 2. The geometry consists of the plenum, combustion chamber, injector and cooling duct (Fig, 3). The combustion chamber and cooling duct are connected via 100 equispaced dilution holes.

We use a half sector geometry because the full geometry is composed of 20 identical sectors and the boundary conditions and volumetric distributions can be imposed exactly with this geometry. The total length of the combustor is 0.5m and the distance between the injector and the choked outlet is 0.3m.

Parameters

The parameters of the thermoacoustic model are reported in Table 1. An ideal gas is assumed, $p_{gas}=\rho_0 r_{gas}T$ to

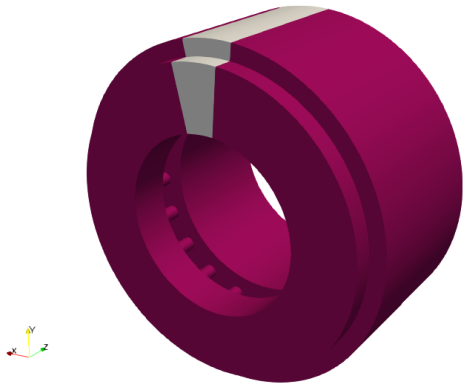

Figure 2. Annular combustor geometry. The gray section represents a single sector out of 20 identical sectors.

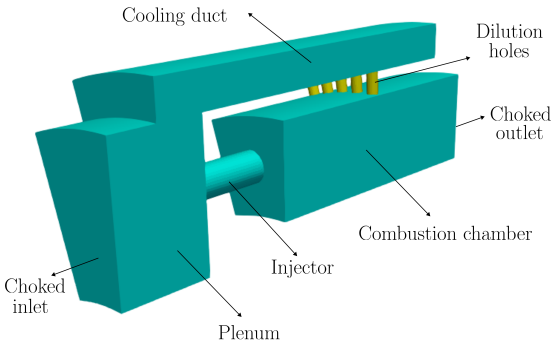

Figure 3. Single sector of the annular combustor. The yellow components show the dilution holes.

Table 1. Dimensional parameters of the thermoacoustic eigenvalue problem

Parameter	value	unit
r_{gas}	287.1	$\mathrm{Jkg^{-1}K^{-1}}$
p_{gas}	5.0	MPa
q_{tot}	-116.161	MW
u_b	193.17	$\mathrm{m\ s^{-1}}$
n	1.0	-
τ	0.0002	s
u_h	8.2751	$\mathrm{m\ s^{-1}}$
L	0.02706	m
σ	0.33	-
M_i	0.03074	-
M_o	0.0702	-

compute the mean density field. The specific heat capacity is assumed to change linearly with the temperature, $c_p(T) = 973.60 + 0.133T$.

Figure 4. Slice of the temperature distribution in the sector. The temperature changes only in the axial direction in order to facilitate comparison with the network model.

The temperature distribution is shown in Fig. 4. The heat release rate distribution (Fig. 5) and measurement function distribution (Fig. 6) are implemented by means of a three dimensional Gaussian function in Eq. (20), where α denotes the standard deviation, which controls the width of the function around point $P(x_0, y_0, z_0)$.

$$G(\mathbf{x}) = \frac{\exp\left((-(x-x_0)^2 + (y-y_0)^2 + (z-z_0)^2)/(2\alpha^2)\right)}{\alpha^3(2\pi)^{3/2}} \tag{20}$$

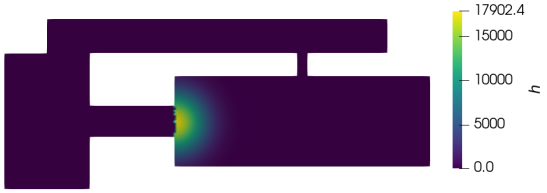

Figure 5. Slice of the heat release rate (h) distribution in the sector. The Gaussian function is defined around the point $P_h = (0, 0.29873, 0.2)$ with $\alpha_h = 0.025$.

Figure 6. Slice of the measurement function (w) distribution in the sector. The Gaussian function is defined around the point $P_w = (0, 0.29873, 0.15)$ with $\alpha_w = 0.005$.

Mesh Dependency

A mesh convergence study is performed to show the influence of the numerical grid on the eigenvalue.

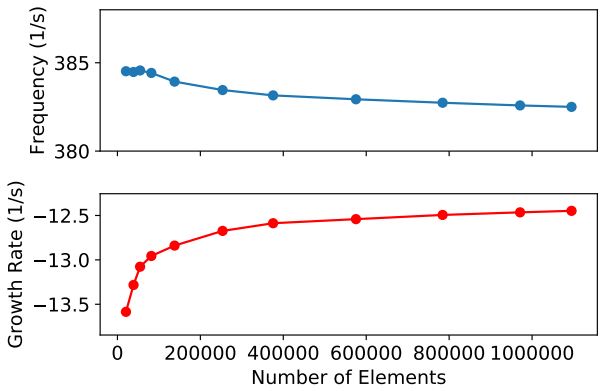

Figure 7. Mesh dependency study for the frequency and growth rate of the passive flame case ($\mathbf{D} = 0$) using the Helmholtz solver with P1 continuous Galerkin elements.

The passive flame configuration is modelled in an industrial thermoacoustic network model, LOTAN (14) which gives an eigenvalue of $390.608 - 10.588j$. From Fig. 7, the eigenvalue computed using the Helmholtz solver converges to $382.502 - 12.544j$ with the same shape eigenmode. Given the significant differences between the network model and the Helmholtz solver, these results are sufficiently close to give us confidence in the Helmholtz solver.

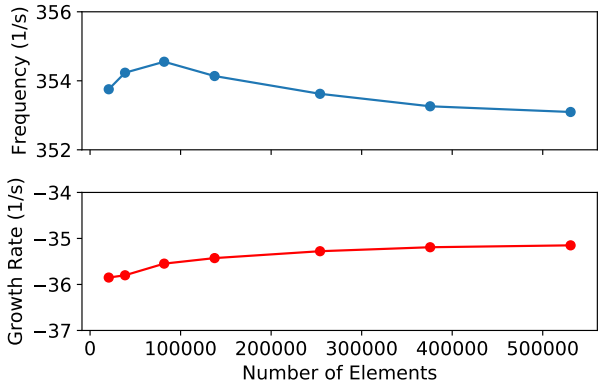

Figure 8. Mesh dependency study for the frequency and growth rate of the active flame case ($\mathbf{D} \neq 0$) using the Helmholtz solver with P1 continuous Galerkin elements.

A similar mesh dependency study is performed for the active flame configuration (Fig. 8). The Helmholtz solver converges to $353.062 - 35.145j$ while LOTAN gives $331.322 - 62.994j$. Again, given the significant difference between the models, this gives us confidence in the Helmholtz solver.

Direct and Adjoint First Axial Eigenmodes

Axial, azimuthal and mixed modes can be calculated with the Helmholtz solver. We present the first axial eigenfunctions of the annular combustor. Fig. 9 and Fig. 10 show the real and imaginary parts of the direct eigenfunction. Similarly, Fig. 11 and Fig. 12 show the real and imaginary parts of the adjoint eigenfunction. We use these eigenfunctions to compute the shape sensitivities using Eq. (19). The direct eigenfrequency is $348.188 - 34.540j$ and the adjoint eigenfrequency is $348.188 + 34.540j$ confirming that they are complex conjugates, as required.

Figure 9. Real part of the first axial direct eigenfunction

Figure 10. Imaginary part of the first axial direct eigenfunction

Figure 11. Real part of the first axial adjoint eigenfunction

Figure 12. Imaginary part of the first axial adjoint eigenfunction

Direct and Adjoint Second Axial Eigenmodes

The other eigenmodes could also effect the acoustic performance of the annular combustor (15). We present the second axial eigenfunctions of the annular combustor. Similar analysis is performed for the second axial eigenmode as for the first axial eigenmode. We calculate the second axial eigenmode of the combustor by changing the target eigenvalue in the Helmholtz solver. Fig. 13 and Fig. 14 show the real and imaginary parts of the direct eigenfunction and Fig. 15 and Fig. 16 show the real and imaginary parts of the adjoint eigenfunction. The direct and adjoint eigenvalues are $700.332 - 6.418j$ and $700.332 + 6.418j$, respectively. The growth rates indicates that the second axial mode is less stable compared to the first axial mode.

Figure 13. Real part of the second axial direct eigenfunction

Figure 14. Imaginary part of the second axial direct eigenfunction

Figure 15. Real part of the second axial adjoint eigenfunction

Figure 16. Imaginary part of the second axial adjoint eigenfunction

The Helmholtz solver can also compute mixed modes as shown in (Fig. 17).

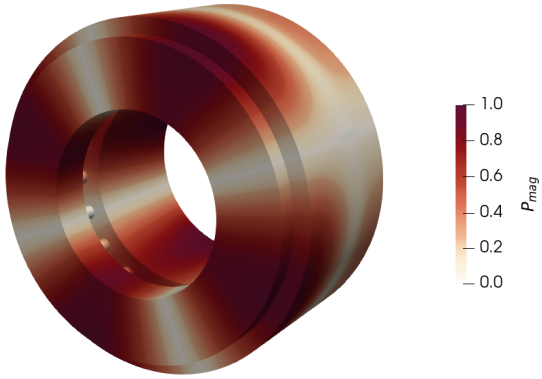

Figure 17. Magnitude of the mixed direct eigenfunction calculated for the passive flame case using the Helmholtz solver. The eigenfrequency for this mode is $755.620268 - 8.680004j$.

Shape sensitivity of the first axial eigenmode

For the first axial mode, we use the direct and adjoint eigenfunctions to calculate the shape derivatives of the surfaces of the combustor. The real and imaginary parts of the shape derivatives represent the influence of the surface displacement on the frequency and growth rate, respectively. The surface sensitivities of the dilution holes are greater than those elsewhere so, for presentation, we scale the shape derivatives by the absolute maximum shape derivative elsewhere.

The shape derivatives for the first axial eigenfrequency is shown in Fig. 18. We observe the shape derivatives are negative for the inlet and outlet choked surfaces. These derivatives demonstrate that the translation of the choked boundaries in the inward surface normal direction increases the eigenfrequency. This is because the frequencies of axial modes depend on the length of the combustor.

Fig. 19 shows the results for the shape derivatives for the the first axial growth rate. As for the shape sensitivity of the eigenfrequency, the largest growth rate sensitivity is observed in the dilution holes. This finding is expected because the Helmholtz solver tries to maximize the volume of the dilution holes in order to increase the damping further. The same effect could be achieved by adding additional dilution holes into the combustor. The growth rate sensitivity for the plenum surfaces are found to be more influential than those of the combustion chamber. Increasing the plenum volume would lead to a more stable system here.

Shape sensitivity of the second axial mode

We repeat the shape sensitivity analysis for the second axial eigenmode. The shape derivatives for the second axial eigenfrequency is shown in Fig. 20. Similary to the shape sensitivity of the first axial frequency, the largest gradients are found on the surfaces of the dilution holes. We observe the shape derivatives are negative for the inlet and outlet choked boundaries, but not as strong as the shape derivatives for the first axial eigenfrequency. This is due to the scaling of the gradients because the shape gradients of the dilution holes are found to be much more larger in the second mode than for the first mode.

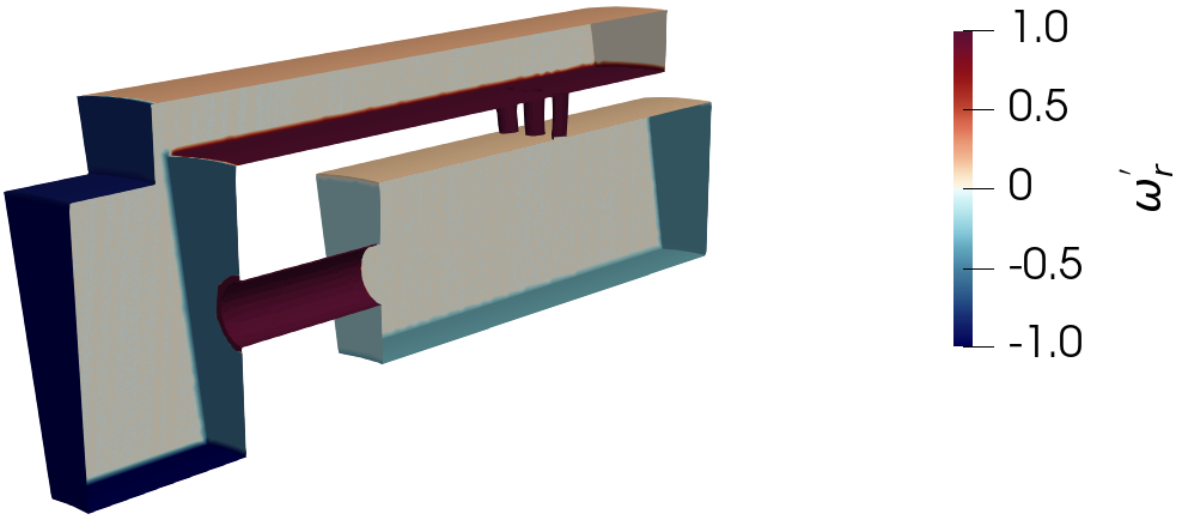

Figure 18. Shape derivatives of the surfaces for sensitivities in the frequency of the first axial mode

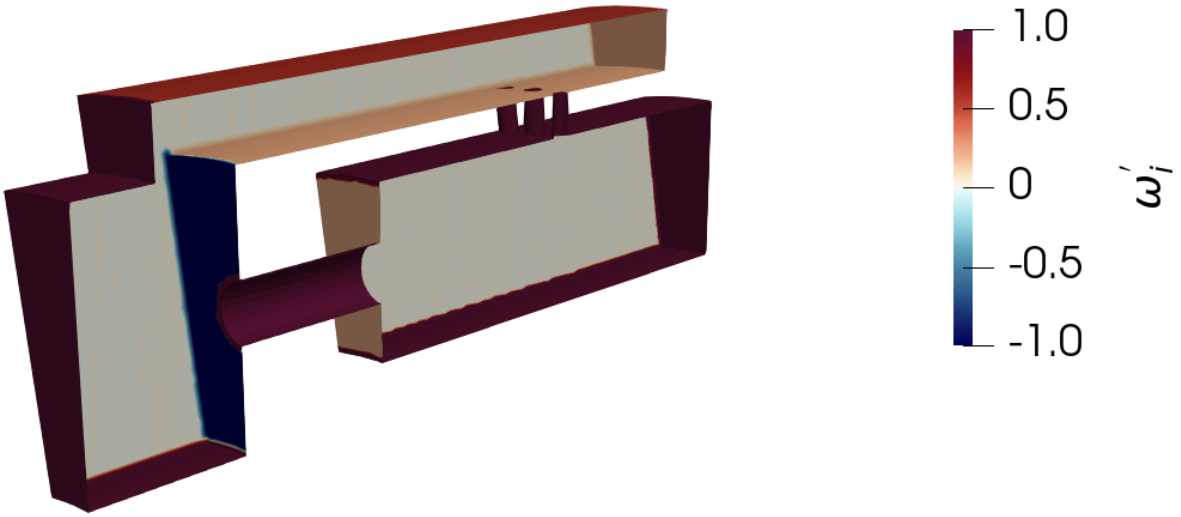

Figure 19. Shape derivatives of the surfaces for sensitivities in the growth rate of the first axial mode

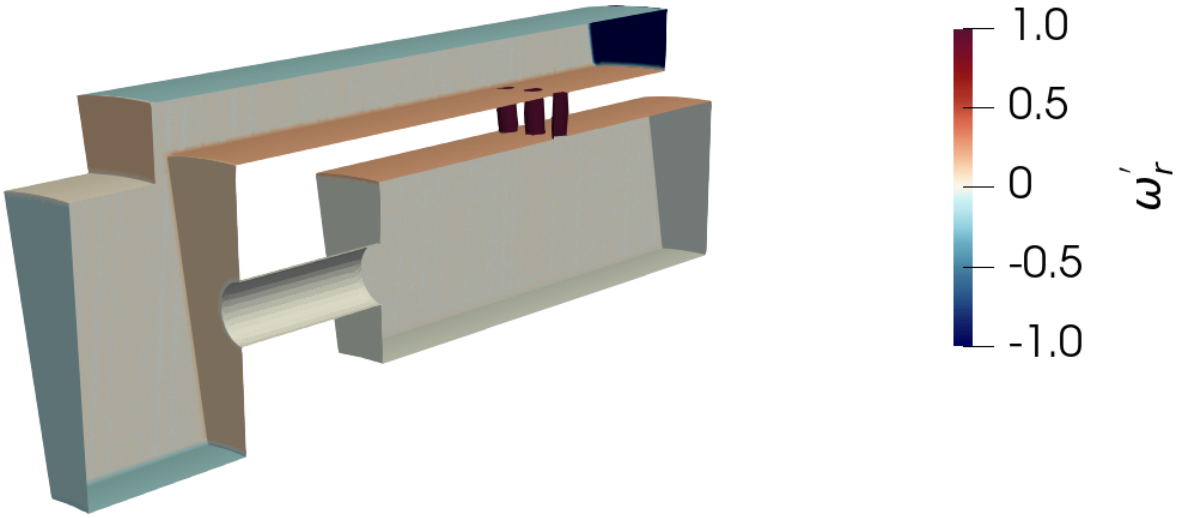

Figure 20. Shape derivatives of the surfaces for sensitivities in the frequency of the second axial mode

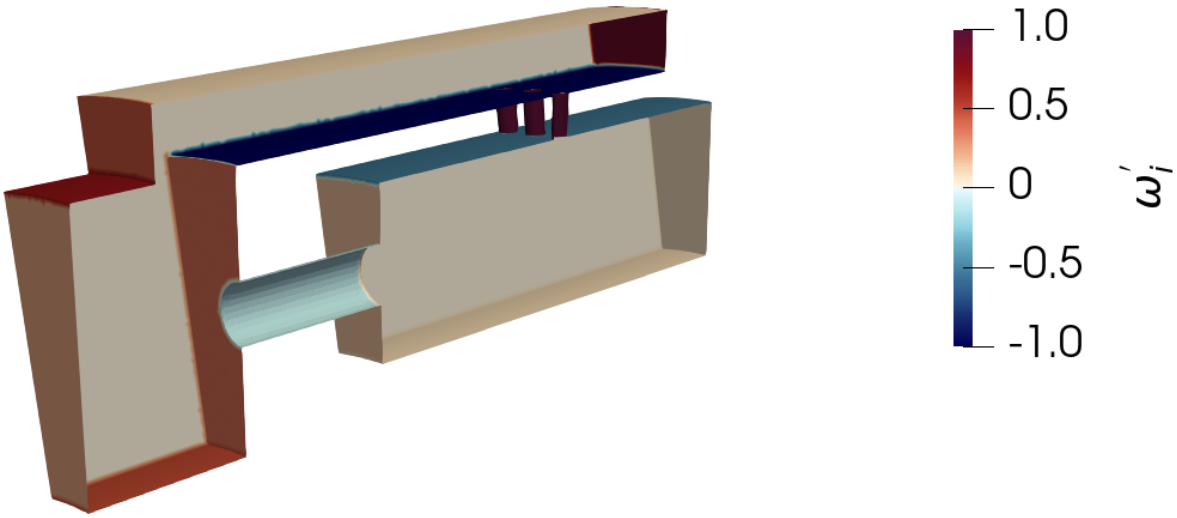

Figure 21. Shape derivatives of the surfaces for sensitivities in the growth rate of the second axial mode

Fig. 21 shows the results for the shape derivatives for the the second axial growth rate. As for the shape sensitivity of the first eigenfrequency, the largest growth rate sensitivity is observed in the dilution holes. The growth rate sensitivity for the cooling duct surfaces are found to be more influential than those of the combustion chamber and the plenum. Reducing the cooling duct volume would stabilize the second mode further.

Conclusion

In this paper, we solve direct and adjoint thermoacoustic Helmholtz equations using a Helmholtz solver with 3D continuous Galerkin finite elements. We implement choked boundaries through reflection coefficients. We incorporate the modified Cummings model to include the damping effect caused by the dilution holes. We also check this model against the industrial thermoacoustic network model LOTAN. The flame response is modelled through a local $n-\tau$ model in which the interaction index, n and the time delay, τ are uniform. We compute the first and second axial direct and adjoint axial eigenmodes of the annular combustor with dilution holes. We then calculate the shape sensitivities of the first and second axial modes of the annular combustor. The surface area of the dilution holes are, unsurprisingly, found to be the most dominant surfaces affecting the eigenfrequency and growth rate for both modes.

By using adjoint methods, computation of shape sensitivity fields becomes relatively cheap for annular combustor geometries with dilution holes. The obtained shape derivatives provide useful guidance about the change of the combustor design to improve thermoacoustic stability for the eigenmodes. The corresponding shape changes informed by the shape derivatives should deal with the multiple eigenmodes.

In future work, we will apply adjoint based shape sensitivity to stabilize more realistic combustor geometries. We will also examine the eigenmodes using more realistic temperature fields and flame transfer functions. In addition to the damping models for the dilution holes, the influence of perforated plates and injectors on the system will be incorporated into the adjoint Helmholtz solver.

Acknowledgements

The authors would like to thank Simon Stow for supplying the industrial code LOTAN and advising on its use. Ekrem Ekici acknowledges funding from Türkiye's Ministry of National Education.

References

[1] Juniper MP. Sensitivity analysis of thermoacoustic instability with adjoint helmholtz solvers. *Physical Review Fluids* 2018; 3(11): 110509.

[2] Magri L. Adjoint methods as design tools in thermoacoustics. *Applied mechanics reviews* 2019; 71(2).

[3] Falco S and Juniper MP. Shape optimization of thermoacoustic systems using a two-dimensional adjoint helmholtz solver. *Journal of Engineering for Gas Turbines and Power* 2021; 143(7).

[4] Aguilar JG and Juniper MP. Thermoacoustic stabilization of a longitudinal combustor using adjoint methods. *Physical Review Fluids* 2020; 5(8): 083902.

[5] Falco S. *Shape optimization for thermoacoustic instability with an adjoint Helmholtz solver*. PhD Thesis, University of Cambridge, 2022.

[6] Surendran A, Na W, Boakes C et al. A low frequency model for the aeroacoustic scattering of cylindrical tube rows in cross-flow. *Journal of Sound and Vibration* 2022; 527: 116806.

[7] Geuzaine C and Remacle JF. Gmsh: A 3-d finite element mesh generator with built-in pre-and post-processing facilities. *International journal for numerical methods in engineering* 2009; 79(11): 1309–1331.

[8] Alnæs M, Blechta J, Hake J et al. The fenics project version 1.5. *Archive of Numerical Software* 2015; 3(100).

[9] Alnæs MS, Logg A, Ølgaard KB et al. Unified form language: A domain-specific language for weak formulations of partial differential equations. *ACM Transactions on Mathematical Software (TOMS)* 2014; 40(2): 1–37.

[10] Balay S, Abhyankar S, Adams M et al. Petsc users manual 2019; .

[11] Hernandez V, Roman JE and Vidal V. Slepc: A scalable and flexible toolkit for the solution of eigenvalue problems. *ACM Transactions on Mathematical Software (TOMS)* 2005; 31(3): 351–362.

[12] Nicoud F, Benoit L, Sensiau C et al. Acoustic modes in combustors with complex impedances and multidimensional active flames. *AIAA journal* 2007; 45(2): 426–441.

[13] Gropp W, Lusk E, Doss N et al. A high-performance, portable implementation of the mpi message passing interface standard. *Parallel computing* 1996; 22(6): 789–828.

[14] Stow SR and Dowling AP. Thermoacoustic oscillations in an annular combustor. In *Turbo Expo: Power for Land, Sea, and Air*, volume 78514. American Society of Mechanical Engineers, p. V002T02A004.

[15] Buschmann PE, Mensah GA and Moeck JP. Intrinsic thermoacoustic modes in an annular combustion chamber. *Combustion and Flame* 2020; 214: 251–262.